JOURNAL OF COMPUTATIONAL PHYSICS 96, 143–162 (1991)

Slanted Conducting Boundaries and Field Emission of Particles in an Electromagnetic Particle Simulation Code*

T. D. POINTON

Sandia National Laboratories, Albuquerque, New Mexico 87185

Received November 15, 1988; revised May 16, 1990

A method to handle slanted perfectly conducting boundaries in electromagnetic particle simulation codes is described. Modifications to standard algorithms for the electromagnetic field advance, charge and current densities, particle destruction, and field averaging are discussed. In addition, a new model for field emission from conducting boundary surfaces is described. Particles can be emitted from conformal or slanted surfaces, and also from certain types of corners. Results of the new models on several problems involving slanted surfaces are presented.

I. INTRODUCTION

Particle-in-cell (PIC) plasma simulation codes are a powerful tool in advancing our understanding of intense, pulsed-power devices. One of the most difficult problems encountered using a PIC code to simulate such a system is the treatment of conducting boundaries and field emission surfaces; many devices have complicated boundary shapes that need to be modeled accurately. The most elegant solution to this problem is to use a non-orthogonal mesh that conforms to the required geometry. Mainly because of difficulties designing a particle handler on such a mesh, it is only recently that success with such methods have been reported [1, 2]. However, most current relativistic electromagnetic PIC codes use an orthogonal grid (often restricted only to Cartesian coordinates) and require that conducting boundaries be conformal to one of the coordinates. With such codes, the only method of simulating a complex boundary shape is to use the closest "stair-step" approximation with conformal segments. On a stair-step surface, the electric field is distorted in both magnitude (enhanced at the outer corners and diminished at the inner corners) and direction (since the tangential component must vanish at each face of the corner). Furthermore, these problems carry over to the field emission of particles. More charge is created at the outer corners, and the

* This work supported by the U.S. Department of Energy under Contract DE-AC04-76-DP00789.

581/96/1-10

0021-9991/91 $3.00

particles follow trajectories determined by the distorted electric field. Although these errors may not affect some of the gross operating characteristics of a device, the behavior close to such surfaces may be quite different from the actual slanted surface being modeled.

This paper describes a method for handling slanted conducting surfaces in an orthogonal mesh code. The method restricts slanted surfaces to those connecting opposite corners of the electromagnetic cell, so it has limited capabilities in comparison with a true body-fitted mesh code. However, the great advantage of this scheme is that it can be added relatively easily to an existing orthogonal mesh code, upgrading its ability to simulate complex geometries for a fraction of the effort required to switch to a non-orthogonal grid. This method has been implemented in the $2\frac{1}{2}$D relativistic electromagnetic PIC code MAGIC [3]. In addition to slanted conducting surfaces, a new field emission model is also described. This model not only supports field emission from conformal and slanted surfaces, but also from certain types of corners. All cells in an emission surface are treated collectively to ensure that the magnitude of the particle charges produce exactly the right amount of charge in each cell, accounting for the area weighting overlap of created particles into adjacent cells.

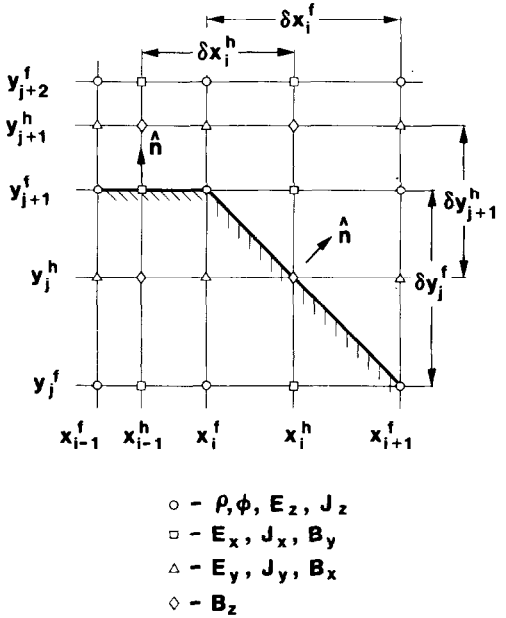

FIG. 1. A section of the spatial grid used for the electromagnetic fields. x_i^f are the "full grid points," and x_i^h are the "half grid points" in the x-direction, and y_j^f and y_j^h are the full and half grid points in the y-direction. The nonuniformity of the grid is greatly exaggerated for illustrative purposes. A conducting surface connects the vertices (x_{i-1}^f, y_{j+1}^f), (x_i^f, y_{j+1}^f), and (x_{i+1}^f, y_j^f), with outward pointing normal as shown.

The organization of this paper is as follows. In Section II, we discuss the treatment of vacuum cells and conformal conducting boundaries. This section defines the notation used and sets the stage for the discussion of slanted surfaces. In Section III, the modifications made to the code for slanted surfaces are described (excluding the particle emission model). In Section IV, a description of the new field emission model is presented. Results of simulations performed with the new code are discussed in Section V. Finally, in Section VI, we summarize the principal results. SI units are used throughout this paper, except where noted.

Two simplifications should be noted in this paper. First, in the interest of notational clarity, the discussion is restricted to Cartesian coordinates. MAGIC handles four different orthogonal coordinate systems—Cartesian, cylindrical $z-r$, cylindrical $r-\phi$, and spherical $r-\theta$. Generalization to the $z-r$ system is straightforward. However, the treatment of the other coordinate systems involves some complications (since the metric tensor coefficients are no longer constants) and is still under development. Second, all discussion of slanted surfaces will be restricted to the orientation shown in Fig. 1, in which both x and y components of the normal vector are positive. Extension to slanted surfaces with normals in the other three quadrants is straightforward.

II. Treatment of Vacuum Cells and Conformal Conducting Boundaries

The spatial grid used for the finite-difference approximation to Maxwell's equations is shown in Fig. 1. Nonuniform grid spacings can be defined to allow better spatial resolution of spatially inhomogeneous quantities with fewer grid points [4]. The "full" and "half" grid points in the x-direction are computed by a mapping from a uniform grid $\zeta_i = i\delta\zeta$, using an arbitrary smooth function g_x; $x_i^f = g_x(\zeta_i)$ and $x_i^h = g_x(\zeta_{i+1/2})$. This means that x_i^h is not necessarily exactly midway between x_i^f and x_{i+1}^f. The full and half grid points in the y-direction, y_j^f and y_j^h, are similarly defined. The staggering of the locations of the field definitions permit simple second-order finite-difference approximations to spatial derivatives to be defined in the usual way [5]. In referring to this grid, we define "full grid point (i, j)" to be the actual point (x_i^f, y_j^f), "full grid cell (i, j)" to be the cell with $x_i^f \leqslant x < x_{i+1}^f$ and $y_j^f \leqslant y < y_{j+1}^f$, and "charge density cell (i, j)" to be the cell with $x_{i-1}^h \leqslant x < x_i^h$ and $y_{j-1}^h \leqslant y < y_j^h$.

Conducting surfaces are defined with vertices at full grid points, together with the direction of the outward pointing normal to orient the surface, as shown in Fig. 1. Slanted surfaces must connect opposite corners of the full grid cell, as shown in the lower right corner of Fig. 1. As pointed out in the Introduction, we will only discuss the treatment for this slanted surface orientation. Two complications arise on a nonuniform grid. First, it is possible for a slanted surface connecting opposite vertices of a full grid cell to miss the grid point near the center of the cell at which B_z is defined. This only affects the special boundary computation of B_z and will be described later; the particle-handling algorithms are unaffected. Second, the slope of

the surface can change from one full grid cell to the next. Although this complicates the coding required to implement the algorithms to be discussed, it also provides the ability to generate piecewise linear approximations to curved surfaces.

Next, we consider the charge density calculation. Since the charge density can vary greatly in time in systems simulated with MAGIC, the simulation particles have variable weights. All particles of the same species have the same charge to mass ratio, but each particle is explicitly assigned its own charge q_p. This can be viewed as explicitly defining how many real particles each simulation particle represents. For a particle located at $\mathbf{x}_p^n = (x_p^n, y_p^n)$ in full grid cell (i, j) at time level n, we define the linear weighting fractions

$$w_{px}^{n+} = \frac{(x_p^n - x_i^f)}{\delta x_i^f}, \qquad w_{px}^{n-} = 1 - w_{px}^{n+},$$
$$w_{py}^{n+} = \frac{(y_p^n - y_j^f)}{\delta y_j^f}, \qquad w_{py}^{n-} = 1 - w_{py}^{n+}. \tag{1}$$

In a vacuum cell, the charge density is accumulated using standard bilinear area

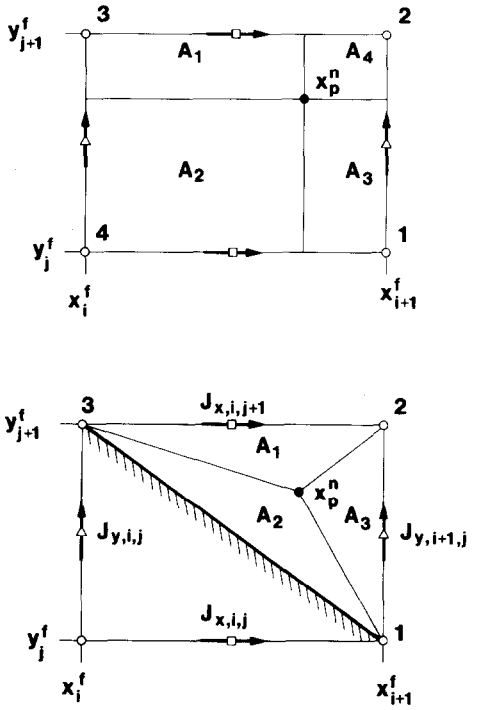

FIG. 2. Charge density weighting for particle p, located in full grid cell (i, j): (a) Rectangular area weighting used in vacuum cells. The fraction of the particle's charge assigned to corner n is proportional to the area of rectangle A_n. (b) Triangular area weighting used in slanted surface cells. The fraction of the particle's charge assigned to corner n is proportional to the area of triangle A_n.

weighting. We divide up the area of the full grid cell into four subrectangles, based on the particle's location, as shown in Fig. 2a. The fraction of the particle charge assigned to the charge density grid point at each corner is proportional to the area of the sub-rectangle opposite that point. These fractions are

$$\begin{aligned} w^n_{p,ij} &= w^{n-}_{px}\, w^{n-}_{py}, \\ w^n_{p,i+1,j} &= w^{n+}_{px}\, w^{n-}_{py}, \\ w^n_{p,i,j+1} &= w^{n-}_{px}\, w^{n+}_{py}, \\ w^n_{p,i+1,j+1} &= w^{n+}_{px}\, w^{n+}_{py}. \end{aligned} \tag{2}$$

At all other grid points (i', j'), $w^n_{p,i'j'} = 0$. The charge density at (i', j') due to particle p is

$$\delta\rho^n_{i'j'} = \frac{q_p w^n_{p,i'j'}}{\delta x^h_{i'}\, \delta y^h_{j'}}. \tag{3}$$

To push the particles, fields are interpolated from the full grid points to the particle using the same weighting factors

$$F_p = \sum_{i',j'} w^n_{p,i'j'} F_{i'j'}. \tag{4}$$

We also need the current density to advance the electric field. A major complication of an electromagnetic PIC code is computing a current density that conserves charge

$$\frac{(J^{n+1/2}_{x,i'j'} - J^{n+1/2}_{x,i'-1,j'})}{\delta x^h_{i'}} + \frac{(J^{n+1/2}_{y,i'j'} - J^{n+1/2}_{y,i',j'-1})}{\delta y^h_{j'}} + \frac{(\rho^{n+1}_{i'j'} - \rho^n_{i'j'})}{\delta t} = 0. \tag{5}$$

MAGIC uses a current density algorithm that satisfies charge conservation exactly, to within machine roundoff error. This algorithm is essentially the "method A" of Ref. [6]. The details of this calculation are quite involved [7], and we simply summarize the results here. First note that for motion confined to a single cell, $\delta\rho/\delta t$ is non-zero only at the four corners of that cell, so one would expect to satisfy continuity everywhere using only the four current densities on the edges of the cell. In fact, since $\sum \delta\rho/\delta t = 0$, there are only three independent equations, and so we have a one parameter family of solutions for these current densities. Two special solutions can be constructed from physical considerations. Consider motion of a particle from $\mathbf{x}^n_p$ to $\mathbf{x}^{n+1}_p$ within a single cell, as shown in Fig. 3. We approximate the actual particle's path with one of the two rectangular paths shown. For illustrative purposes, we will assume this to be path 1, where the y-direction is traversed first. As the particle traverses the segment parallel to the y-axis, the y-component of the current is

$$I^{n+1/2}_{py} = q_p(y^{n+1}_p - y^n_p)/\delta t. \tag{6}$$

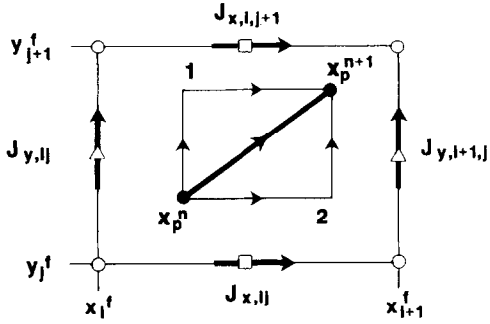

FIG. 3. Current density calculation for motion confined to a single cell. The particle's path from $\mathbf{x}_p^n$ to $\mathbf{x}_p^{n+1}$ is approximated by one of the two rectangular paths shown. This motion contributes to the current densities only on the four edges of cell.

This current is shared between $J_{y,ij}^{n+1/2}$ and $J_{y,i+1,j}^{n+1/2}$, using a transverse weighting factor that depends on the x-location of the path. Along the chosen path, we assign w_{px}^{n-} of the current to $J_{y,ij}^{n+1/2}$ and the remaining w_{px}^{n+} to $J_{y,i+1,j}^{n+1/2}$. Dividing by the cell volumes, the current density contributions are

$$J_{y,ij}^{n+1/2} = \frac{q_p w_{px}^{n-}(w_{py}^{n+1,+} - w_{py}^{n+})}{\delta t\, \delta x_i^h},$$
$$J_{y,i+1,j}^{n+1/2} = \frac{q_p w_{px}^{n+}(w_{py}^{n+1,+} - w_{py}^{n+})}{\delta t\, \delta x_{i+1}^h}. \tag{7}$$

The x-component of the current is treated similarly, except that the transverse weighting factors are $w_{py}^{n+1,\pm}$, since the x-motion is made at y_p^{n+1} on the chosen path. These current density components are

$$J_{x,ij}^{n+1/2} = \frac{q_p w_{py}^{n+1,-}(w_{px}^{n+1,+} - w_{px}^{n+})}{\delta t\, \delta y_j^h},$$
$$J_{x,i,j+1}^{n+1/2} = \frac{q_p w_{py}^{n+1,+}(w_{px}^{n+1,+} - w_{px}^{n+})}{\delta t\, \delta y_{j+1}^h}. \tag{8}$$

It is straightforward to verify that these current densities do in fact satisfy Eq. (5) at all points. If the other path is chosen, the only difference is that the transverse weights for J_y are $w_{px}^{n+1,\pm}$, and those for J_x are $w_{py}^{n\pm}$. Any weighted average of these two solutions is also a solution. In MAGIC, one or the other is chosen randomly. For particles making cell transitions, we exploit the linearity of the continuity equation by dividing up the particle's path into segments confined to a single cell, and treating each segment separately, using the method just described.

The treatment of the electromagnetic fields at perfectly conducting conformal boundaries is straightforward. Only fields actually on the surface need to be

modified. Consider a conductor conformal with x (i.e., $x = \text{const}$). After the standard field advance has been made, we perform a boundary correction, setting E_y, E_z, and B_x equal to zero on the surface. Similarly, after the standard current density accumulation, we set $J_y = 0$. With these modifications, charge conservation and Gauss' Law are no longer satisfied at full grid points on the conductor, but this is not a problem. Charge needs to be rigorously conserved only at interior grid points. The treatment of particles which cross the boundaries will be discussed below.

III. Modifications for the Treatment of Slanted Surface Cells

In this section, we describe the changes made to handle slanted surface cells, excluding the particle creation model. The principal changes are in advancing the electromagnetic field, computing charge and current densities that satisfy charge conservation, destroying particles that pass through these surfaces, and averaging the electromagnetic fields for the particle pusher.

We first consider the modifications for the electromagnetic field calculation. As with conformal conducting boundaries, to correct the field solver at a slanted surface, only fields actually on the surface need to be modified, i.e., E_z and B_z. To satisfy $E_{\tan} = 0$, we set $E_z = 0$. For B_z in the center of full grid cell (i, j) in Fig. 1, we apply the integral form of Faraday's law to the triangular loop formed by the vertices (x_i^f, y_{j+1}^f), (x_{i+1}^f, y_{j+1}^f) and (x_{i+1}^f, y_j^f), to give the simple rule for advancing this field in time by δt

$$\delta B_{z,ij} = \frac{2\,\delta t}{\delta y} E_{x,i,j+1} - \frac{2\,\delta t}{\delta x} E_{y,i+1,j}. \tag{9}$$

Strictly speaking, this increment is correct to second order in δx and δy only if the grid point at which B_z is located is exactly at the center of the full grid cell. However, the additional errors incurred in simply using Eq. (9) for a nonuniform grid are small, and do not warrant a more elaborate procedure.

We next consider the charge and current densities. The treatment of slanted surface cells is a natural geometric extension of the area weighting scheme [8] illustrated in Fig. 2b. The particle contributes to the charge density only at the three vertices in the vacuum half of the cell. The triangular area of the vacuum half of the cell is divided up into three subtriangles, based on the particle's location, and the fraction of the particle's charge assigned to each charge density cell is proportional to the area of the sub-triangle opposite that corner. This leads to the particle weights

$$\begin{aligned} w_{p,i+1,j}^n &= w_{py}^{n-}, \\ w_{p,i,j+1}^n &= w_{px}^{n-}, \\ w_{p,i+1,j+1}^n &= w_{px}^{n+} - w_{py}^{n-}, \end{aligned} \tag{10}$$

where $w_{px}^{n,\pm}$ and $w_{py}^{n,\pm}$ are defined in Eq. (1). The "rectangular" weights in a vacuum cell and the "triangular" weights for a slanted surface cell vary continuously as a particle crosses the cell boundary between the two.

For the current density, the perfect conductor boundary condition forces $J_{x,ij}$ and $J_{y,ij}$ to be zero. The continuity equation at the three vacuum corners of the slanted cell gives three equations for the two unknown current terms $J_{x,i,j+1}^{n+1/2}$ and $J_{y,i+1,j}^{n+1/2}$. As in the rectangular case, these equations are not independent. There are only two independent equations, and it is easily verified that continuity is satisfied at all points with the current densities

$$J_{x,i,j+1}^{n+1/2} = \frac{q_p(w_{px}^{n+1,+} - w_{px}^{n+})}{\delta t\, \delta y_{j+1}^h},$$
$$J_{y,i+1,j}^{n+1/2} = \frac{q_p(w_{py}^{n+1,+} - w_{py}^{n+})}{\delta t\, \delta x_{i+1}^h}. \tag{11}$$

Comparison of Eq. (11) with Eqs. (7) and (8) shows that these terms are almost identical to the current density terms for a vacuum cell, the only difference being that the transverse weighting factors are set to zero for the edge below the surface, and unity for the edge above, independent of the particle location or rectangular path chosen.

When a particle penetrates a conductor or the edge of a simulation region following the particle push at a given time step, it is immediately removed from the system and makes no contribution to the new charge density ρ^{n+1}. However, as the particle moves along its path from time step n to $n+1$, motion along the portion of the path within the vacuum cell makes a contribution to $\mathbf{J}^{n+1/2}$ that must be included to conserve charge. In the old version of MAGIC, only conformal boundaries were encountered, and all contributions to the current density from motion outside the system were simply confined to edges of "destruction" cells, i.e., cells immediately below the conducting boundary. The unwanted current contributions could be removed with a simple boundary correction on these cells, and no truncation of particle paths was necessary. This simple approach can no longer be used when slanted surfaces are present. There is no way to separate contributions to the current density from motion in the vacuum and destruction halves of a slanted surface cell. The only way to correctly compute the current is to explicitly truncate the path at the slanted surface. Furthermore, because of complications near conformal/slanted corners, it is not worth the trouble of using the old algorithm on conformal surfaces. Thus all particle paths which intersect boundary surfaces are truncated at the intersection point. These particles are then destroyed after their contribution to the current density is computed.

Finally in this section, we describe the modifications made for the field averaging used by the particle pusher. The staggered spatial locations of the electromagnetic fields are convenient for advancing them forward in time. However, it is inconvenient to work directly with these fields for the particle pusher, since several sets

of weighting coefficients would be required for each particle. Instead, once the fields have been computed on the spatial grid, "average" fields are computed at the full grid points. This allows the charge density weights to be used to interpolate all fields from the grid to each particle, using Eq. (4). The particles are pushed using rectangular weights in vacuum cells and triangular weights in slanted surface cells.

Figure 4 shows the fields on the electromagnetic grid which contribute to the average fields at grid point (i, j). We first consider the case of a uniform grid as shown here. The average electric field must satisfy $E_{\tan} = 0$, so $E^{\text{av}}_{z,ij} = 0$. $E^{\text{av}}_{x,ij}$ and $E^{\text{av}}_{y,ij}$ are computed from $E_{x,ij}$, $E_{x,i-1,j+1}$, $E_{y,ij}$, and $E_{y,i+1,j-1}$, which all lie on the line passing through the points (x_i^f, y_j^h) and (x_i^h, y_i^f). This line, loosely referred to as the line "half a cell above the slanted surface," has slope $\delta y_j^h / \delta x_i^h$ and is located at height

$$\delta h = \tfrac{1}{2}\, \delta x_i^h\, \delta y_j^h ((\delta x_i^h)^2 + (\delta y_j^h)^2)^{-1/2} \tag{12}$$

above the surface. The point P in Fig. 4 is the intersection of this line with the normal to it that passes through (x_i^f, y_j^f). We first compute values of E_x and E_y at P, using linear interpolation from the two nearest components on the line half a cell above the surface

$$\begin{aligned} E_{x,P} &= \frac{d_{12}}{(d_{11}+d_{12})} E_{x,i-1,j+1} + \frac{d_{11}}{(d_{11}+d_{12})} E_{x,ij}, \\ E_{y,P} &= \frac{d_{22}}{(d_{21}+d_{22})} E_{y,ij} + \frac{d_{21}}{(d_{21}+d_{22})} E_{y,i+1,j-1}, \end{aligned} \tag{13}$$

where d_{11}, d_{12}, d_{21}, and d_{22} are the distances shown in Fig. 4. While this averaging

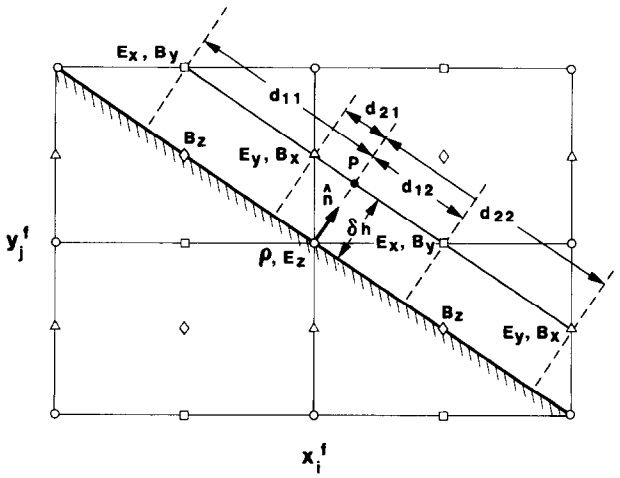

FIG. 4. Computation of the average fields at a slanted surface. Only the field components which are explicitly labelled contribute to the average fields at full grid point (x_i^f, y_j^f).

may seem somewhat arbitrary, it is actually the degenerate case of triangular area weighting when the point being weighted lies on the diagonal of the cell. $E_{x,P}$ given by Eq. (13) is precisely that obtained from $E_{x,ij}$, $E_{x,i-1,j+1}$, and $E_{x,i,j+1}$ using triangular area weighting. Thus this field weighting is consistent with the particle weighting. The normal field at P is obtained from $E_{x,P}$ and $E_{y,P}$ and extrapolated down to the surface by application of Gauss' Law

$$E_{n,\mathrm{sur}} = E_{n,P} - \rho_{ij}\,\delta h/\varepsilon_0. \tag{14}$$

$E^{\mathrm{av}}_{x,ij}$ and $E^{\mathrm{av}}_{y,ij}$ are then defined as the components of $E_{n,\mathrm{sur}}$. For a nonuniform grid, we use exactly the same procedure. The distances δh, d_{11}, d_{12}, d_{21}, and d_{22} are all defined in terms of δx_i^h and δy_j^h as if the grid were uniform, and the point P is defined as before. Although the grid points at which the electric field components are defined may lie slightly off the line half a cell above the surface, the additional errors this incurs are negligible in practice.

The boundary condition for the magnetic field is $B_{n,\mathrm{sur}} = 0$. $B^{\mathrm{av}}_{z,ij}$ is computed from $B_{z,i-1,j}$ and $B_{z,i,j-1}$ using linear weighting along the slanted surface, in a manner very similar to the way $E_{x,P}$ and $E_{y,P}$ are computed in Eq. (13). The tangential component of B is in the $x-y$ plane on the surface is computed by first computing this component at the point P. First, $B_{x,P}$ and $B_{y,P}$ are calculated in the same way as $E_{y,P}$ and $E_{x,P}$, respectively. The resulting value of $B_{\tan,P}$ computed from these components is then is extrapolated down to the surface neglecting corrections due to J_z in Ampere's law; i.e., we simply set $B_{\tan,\mathrm{sur}} = B_{\tan,P}$.

IV. Field Emission Model

The details of field emission of charged particles from an electrode are very complicated [9]. However, most are on length scales too small ($\sim 10^{-4}$ cm) to be resolved with typical cell sizes used in MAGIC. Instead, only the macroscopic effects of field emission are simulated. These can be summarized by the following two-step process. Once the normal electric field exceeds a threshold breakdown field $E_{\mathrm{BD}} \sim 10^7$ V/m, a dense plasma quickly forms on the conducting surface. Subsequent particle emission is from the outer surface of the plasma. The magnitude of the emitted current is space-charge limited, i.e., enough current is drawn to force

move away from the surface at the ion sound velocity, it stays very close to the surface on time scales typically simulated with MAGIC ($\sim$10–100 ns).

The new field emission algorithm is based on a simple application of Gauss' law to cells on the surface of a conductor, as done in some previous work on field emission models [3, 10]. Assuming that the normal component of **E** is zero on the conductor surface, the surface integral of **E** over the remaining faces of a surface cell gives how much charge is required in the cell to actually force this condition. The difference between this charge and that currently in the surface cell is how much

needs to be created. New particles are created to supply this charge, assuming it has the same sign as the species being emitted. These particles are emitted directly from the conductor surface; no explicit treatment of the plasma near the surface is made, since its thickness is assumed to be very small compared to a cell size. In MAGIC, a threshold electric field can be defined to disable emission until the normal field first exceeds it. However, rather than trying to model the breakdown process more carefully, this is primarily a numerical switch to avoid creating and pushing low weight particles early in a simulation (MAGIC's adjustable particle weights can be arbitrarily small). Typical simulations involve driving a system with an input wave that ramps up linearly in time to some value and is constant thereafter. In this case, the final equilibrium state is independent of the code's breakdown threshold as long as this field is much less than the final vacuum field strength of the input wave.

To construct general emission surfaces, we use five types of emission cells, as shown in Fig. 5. Each cell type has four possible orientations. The shape of the emission cells is essentially arbitrary and is determined as follows. First, the natural definition of an emission cell at grid point (i, j) on a conformal boundary is the

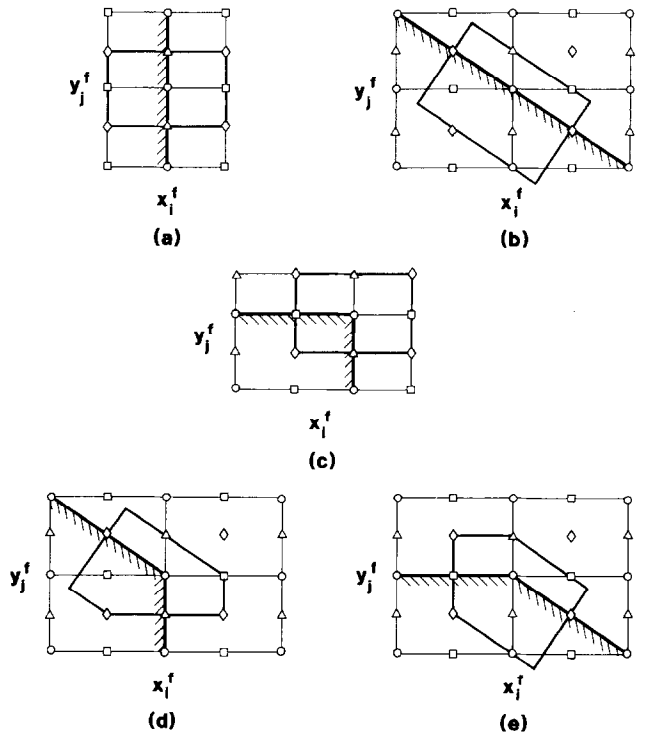

FIG. 5. The five types of surface cells used in the particle emission model: (a) conformal surface; (b) slanted surface; (c) conformal/conformal corner; (d) conformal-x/slanted corner; and (e) conformal-y/slanted corner.

charge density cell at that point. On a uniform grid, as shown in Fig. 5, the other cell shapes follow as logical, but arbitrary, choices that connect smoothly to the conformal surface emission cells. To generalize to a nonuniform grid, each shape is defined as in the uniform case, but with the local values of δx_i^h and δy_j^h. This means that slanted surface cells may not line up exactly, but this is another additional small error incurred in treating slanted surfaces on a nonuniform mesh. In practice, no problems have been seen with this approach. An emission surface is built up as an oriented contiguous chain of these basic cell types. We define the positive direction of traversal as the one going around the conductor counterclockwise (equivalently, if one goes around the outside of the conductor in the positive sense, the conductor is on the left). With these cell types, most types of emitting conductors can be simulated directly.

The creation algorithm must compute how much charge to create in the cell (if any), and the coordinates, momenta, and charges of the created particles (recall that MAGIC must explicitly define the particle charges). Furthermore, the electric field components near the surface must be modified when particles are created to ensure that no interior grid point is a source of charge. We now consider these problems in more detail.

We consider an arbitrary emission cell, labelled with index l, located at grid location (i, j). The amount of charge to be created in this cell, $Q_{cr,l}$, is computed by applying Gauss' law

$$\varepsilon_0 \int_l \mathbf{E} \cdot \mathbf{dA} = \int_l \rho \, dV + Q_{cr,l}, \tag{15}$$

where $\mathbf{E}$ and ρ are the fields before creating particles, and the electric field surface integral is only over the outer surface of the cell. Strictly speaking, the charge-conserving field corrections for the created particles should be included in Eq. (15), but this is a minor correction which can be neglected. The surface integral is computed as

$$\int_l \mathbf{E} \cdot \mathbf{dA} = \sum_{s=1}^{n_s} E_{n,ls} \, \Delta A_{ls}, \tag{16}$$

where n_s is the number of segments on the outer surface (1 for a conformal or slanted cell, 2 for a corner cell), ΔA_{ls} is the surface area of the sth segment of the outer surface, and $E_{n,ls}$ is the outward pointing normal electric field at the center of the sth segment. The charge density integral is defined as

$$\int_l \rho \, dV = Q_l = \sum_{i',j'} V_{i'j'} \rho_{i+i',j+j'}, \tag{17}$$

where $V_{i'j'}$ is the volume overlap of creation cell l into charge density cell $(i+i', j+j')$. For conformal surfaces and conformal/conformal corners, these calculations are trivial. The normal field terms in Eq. (16) come directly from the

grid, and we only have the center term ($i'=0$, $j'=0$) in the sum (17). For example, for the conformal/conformal corner of Fig. 5c

$$Q_{cr,l}=\varepsilon_0(E_{x,ij}\,\delta y_j^h+E_{y,ij}\,\delta x_i^h)-\rho_{ij}\,\delta x_i^h\,\delta y_j^h. \tag{18}$$

The slanted cell calculation is illustrated in Fig. 6. For the surface integral of the field, the normal field at the center of the outside face of the cell is obtained from the four field components shown, in exactly the same way as $E_{n,P}$ in the average field calculation described in Section III. The slanted surface cell has triangular volume overlaps in the four adjacent charge density cells, but only the V_{00}, V_{10}, and V_{01} terms are non-zero. The extension to the treatment of slanted/conformal corners is straightforward.

In MAGIC, the user specifies how many particles to create in each cell. Regardless of cell type, all particle coordinates are generated from two parameters—s_{tran}, a dimensionless fraction from zero to one representing the transverse location of the particle within that cell, and δh, the normal height from the surface at that transverse location. The user specifies whether these parameters are chosen randomly or systematically. For conformal and slanted surface cells, s_{tran} is simply proportional to the transverse distance from the leading edge of the cell (this edge is unique since we sweep through the cell with the positive direction of the traversal). At a corner, a smooth transition of coordinates and momenta from one face of the corner to the other is accomplished by effectively emitting the particles from the surface of a hyperbola fitted to the corner. Figure 7 shows a hyperbola fitted to a corner of angle $2\theta_0$ in which one of the asymptotes is the x-axis. From a standard representa-

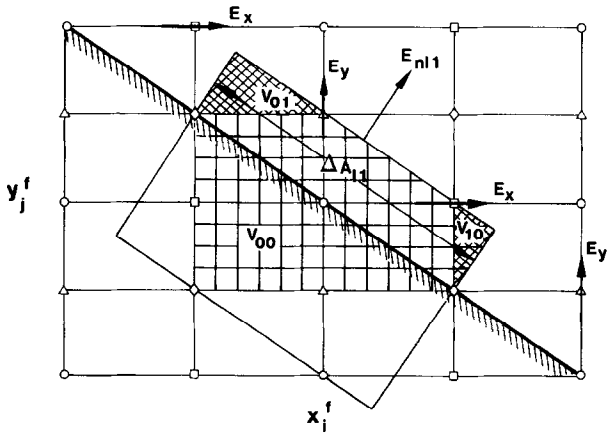

FIG. 6. Calculation of a charge to create in a slanted surface cell. The four electric field components labelled with arrows are used for the normal field. The amount of charge already in the cell is computed from the charge density at full grid points (i, j), $(i+1, j)$, and $(i, j+1)$, using the volume overlaps V_{00}, V_{10}, and V_{01}, respectively.

tion of a hyperbola in polar coordinates [11], we derive the useful parametric representation of this hyperbola,

$$r(\theta) = \frac{a \tan^2 \theta_0}{1 + \cos\theta + \sin\theta \tan\theta_0},$$
$$x(\theta) = r\cos\theta - a, \tag{19}$$
$$y(\theta) = r\sin\theta - a\tan\theta_0,$$

where r and θ are the radius and angle relative to the hyperbola focus, and a is the distance of closest approach of the hyperbola to the corner vertex, as shown. This representation is valid in the range $2\theta_0 - \pi < \theta < \pi$. The outward pointing unit normal to the hyperbola is given by

$$\hat{\mathbf{n}}(\theta) = N_0(1 + \cos\theta, \sin\theta + \tan\theta_0), \tag{20}$$

where N_0 is a normalization coefficient. To fit such a hyperbola to an emitting corner cell, one free parameter θ_0 is fixed by the angle of the corner. The other parameter a is adjustable. For small a, the hyperbola is fitted tightly to the corner, with the slope very close to that of each surface at the ends of the cell (i.e., the parts of the cell furthest from the corner). However, points equally spaced in θ become bunched at the corner itself. Although this can be used beneficially to model enhanced emission at a corner, if a is too small all the particles will be emitted close to the corner itself. On the other hand, if a is large, the bunching at the

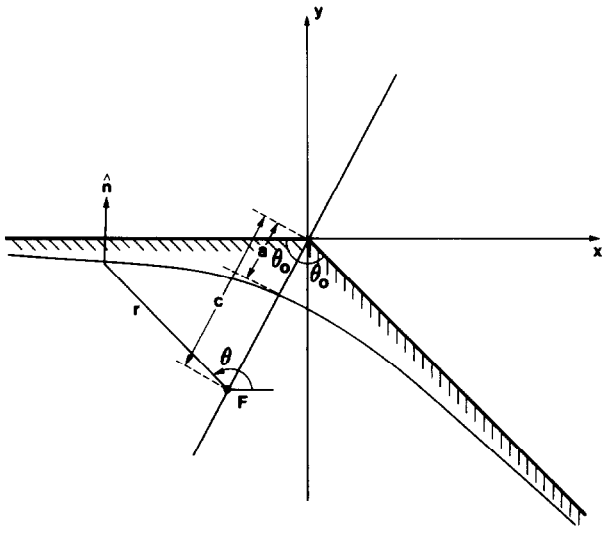

FIG. 7. Hyperbola fitted to a corner of angle $2\theta_0$ at the origin. The distance of closest approach to the origin is a, and the distance from the origin to the focus, F, is $c = a/\cos\theta_0$.

corner is reduced, but the difference between the slope of the hyperbola and the corresponding surface at the ends of the cell increases. In practice, the best compromise appears to be for a being 0.2 times the length of the diagonal of the full grid cell at the corner. A particle is emitted from a point on the hyperbola corresponding to $\theta(s_{\text{tran}})$, along the ray parallel to the normal at this point and at a height δh above the point at which this ray intersects the actual conductor surface.

The momentum direction of each created particle is well defined, since it is emitted with momentum normal to the surface in conformal and slanted surface cells, or along the normal to the hyperbola in corner cells (with a possible thermal spread). However, the momentum magnitude is a free parameter. At a truly space-charge-limited emitting surface, the normal electric field is zero, and particles are emitted with zero velocity, but leave the surface because the field gradient is singular. In a PIC code, the field gradient is necessarily finite, so particles must be created above the surface with a non-zero velocity to enter the system. Currently,

[redacted]

this code is used.

We next consider the computation of particle charges. The amount of charge to create in the cell $Q_{cr,l}$ is given by Eq. (15), while the number of particles and their locations are determined as described above. We must compute the magnitude of the particle charges to create the correct amount of charge in each cell. Because of the charge weighting scheme used in MAGIC, a particle created at a surface cell actually contributes charge to either three or four grid points. In particular, this particle will contribute a charge to one of the two neighboring emitting surface cells. If the charge to be created in each surface cell is different, this coupling between nearest neighbors must be included to force the normal field at the surface to vanish exactly in each cell.

The emission surface has N_c cells C_l, with charge $Q_{cr,l}$ to be created in each cell. This charge is to be supplied by N_p particles created over the surface, with $N_{p,l}$ particles in cell C_l. Particle p in cell C_l has charge q_{lp}, and contributes a fraction of this charge A_{lmp} to cell C_{l+m}. These fractions are the same charge density weighting factors described previously, but with indices specific to the cells on the emitting surface. With linear weighting, $A_{lmp}=0$ for $|m|>1$. We arbitrarily choose one charge from each cell, label it q_{l1}, and define weights $w_{lp}=q_{lp}/q_{l1}$. These weights are defined externally by the user at the start of the problem. Typically, all particles created in a cell will have the same charge, so that $w_{lp}=1$; but for certain problems, it is convenient to allow the more general case. The total charge in cell l due to particles created in cell $l+m$ is $Q_{lm}=S_{lm}q_{l+m,1}$, where

$$S_{lm}=\sum_{p=1}^{N_{p,l+m}} A_{l+m,-m,p}w_{l+m,p}. \tag{21}$$

Summing up the contributions of the three cells which contribute charges to cell l gives the linear equations

$$S_{l,-1}q_{l-1,1} + S_{l,0}q_{l,1} + S_{l,+1}q_{l+1,1} = Q_{cr,l}. \tag{22}$$

Equation (22) is a simple tri-diagonal linear system for the N_c unknowns q_{l1}, which can be solved very rapidly. The other particle charges are then computed using the known weights w_{lp}.

In addition to creating a charge in neighboring surface cells, a particle created in a surface cell contributes a charge to interior charge density grid points next to the surface. If Gauss' law was satisfied before this charge was introduced, it is clearly not satisfied afterwards, so we must correct the electric field near the surface after the particles have been created, so that Gauss' law is again satisfied at all interior points. In both the rectangular and triangular weighting schemes, a particle right on the surface does not contribute a charge to the interior points of the cell. We can therefore satisfy Gauss' law exactly by the following conceptual two-step process. We "create" the particle on the surface and then move it up to its actual creation point in time δt with the standard algorithm. The charge-conserving property of the current density algorithm provides exactly the required field corrections. In practice, these field corrections are computed directly in the particle creation routine.

V. Results

The first series of tests were on simple one-dimensional systems—the monopolar and bipolar planar diodes. Two parallel infinite plane conductors are separated by a distance d, and the potential difference between the two is held at V_0. In the monopolar case, only the cathode emits electrons, while in the bipolar case, ions are also emitted from the anode. These problems have simple solutions for space-charge-limited emission equilibria [12], and simulations of them give good quantitative information on the code's performance. Extensive tests [7], using both conformal and slanted surfaces, provided confidence that the code was working well.

Results of the monopolar planar diode using slanted surfaces are presented here. The simulation geometry is shown in Fig. 8. This geometry requires the grid to be uniform. The "shifted" periodic boundaries enforce the condition, $F(x + L_x, y - L_y) = F(x, y)$, for any field F. Furthermore, when a particle leaves the right-hand boundary, its coordinates are shifted by the vector $(-L_x, L_y)$. The equilibrium electron current is [12]

$$j_0 = \frac{4}{9}\varepsilon_0 \left(\frac{2e}{m}\right)^{1/2} \frac{V_0^{3/2}}{d^2}. \tag{23}$$

Three sets of simulations were performed, each one with fixed d, V_0, and slant

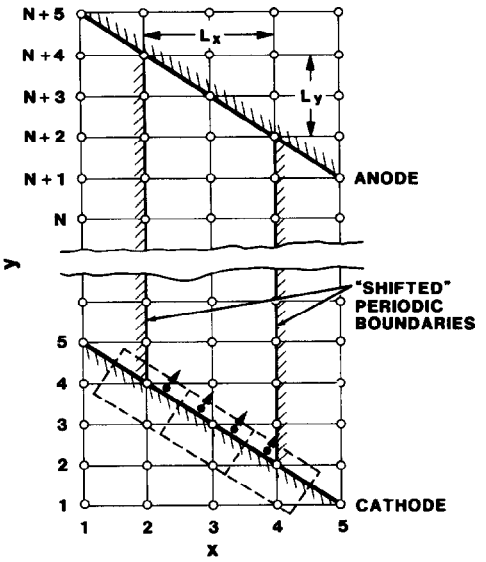

FIG. 8. MAGIC simulation geometry used for the slanted surface Child–Langmuir tests. The slanted surfaces are perfect conductors. The left and right boundaries are periodic boundaries, which require a buffer cell on each side of the simulation system. Particles are emitted as shown.

angle. The three angles used corresponded to the cell sizes $\delta x = \delta y$, $\delta x = 2\,\delta y$, and $\delta x = 4\,\delta y$. The three systems simulated had the parameters shown in Table I.

For each system, three simulations were performed with the number of cells across the gap N being 20, 40, and 80. The Courant condition on the time step [5] requires $\delta t \propto 1/\delta x \propto 1/N$. Particles were created at every time step, so the total run time was proportional to N^2. The simulation results are shown in Table II. These results show that the slanted emission model is fairly insensitive to slant angle, at least over the range covered here. The error in the equilibrium current is comparable to the results for conformal surfaces.

Several real experimental devices have been simulated with the code. No major

TABLE I

The Three Monopolar Diode Parameter Sets Used in the Slanted Surface Child–Langmuir Tests

$\delta x/\delta y$	d(mm)	V_0(kV)	j_0(MAm^{-2})
1	1.414	50	13.0
2	1.789	50	8.14
4	1.940	50	6.92

TABLE II

Simulation Results of the Three Slanted Surface Monopolar Diode Configurations Shown in Table I, with 20, 40, and 80 Cells across the Gap

$\delta x/\delta y$	N	$j_x(\mathrm{MAm}^{-2})$	$j_y(\mathrm{MAm}^{-2})$	$j(\mathrm{MAm}^{-2})$	% error
1	20	9.64	9.67	13.7	5.0
1	40	9.38	9.37	13.3	2.0
1	80	9.26	9.28	13.1	0.8
2	20	3.81	7.63	8.53	4.8
2	40	3.71	7.40	8.28	1.7
2	80	3.66	7.32	8.18	0.5
4	20	1.75	7.01	7.23	4.4
4	40	1.71	6.83	7.04	1.8
4	80	1.69	6.75	6.96	0.6

problems have been found, though it can be quite difficult to quantitatively evaluate the results, since the experimental data is sensitive to many factors, some beyond the scope of MAGIC. As an illustration of these full two-dimensional simulations, we present results of a simulation of the HELIA diode [13] with a tapered cathode. This system is shown in Fig. 9. In this simulation, only electrons were emitted. The input voltage pulse was linearly ramped from zero to its maximum value of 4 MV in 1 ns and held constant for the remaining 9 ns of the simulation. The equilibrium voltage and total current were 3.2 MV and 150 kA, respectively, in good agreement with experiment. Figure 10 is an electron trajectory plot after 5000 time steps, at $t = 10$ ns. The fact that the trajectories of the electrons leaving the cathode are still laminar is a strong indication that there are no problems with the treatment of the boundaries. The greater density of simulation particles at the corners is due to the fact that four times as many particles are emitted from corner cells, to more

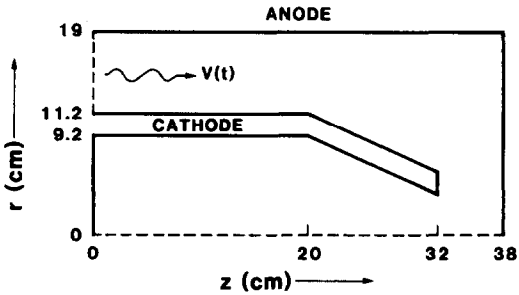

FIG. 9. Tapered cathode HELIA diode configuration used for the simulation described in Section V. The top and right boundaries are the perfectly conducting anode. The gap between the anode and cathode on the left edge is open to the propagation of electromagnetic waves. The input driver wave, incident from the left, and scattered waves propagating backwards from the right, pass through this boundary.

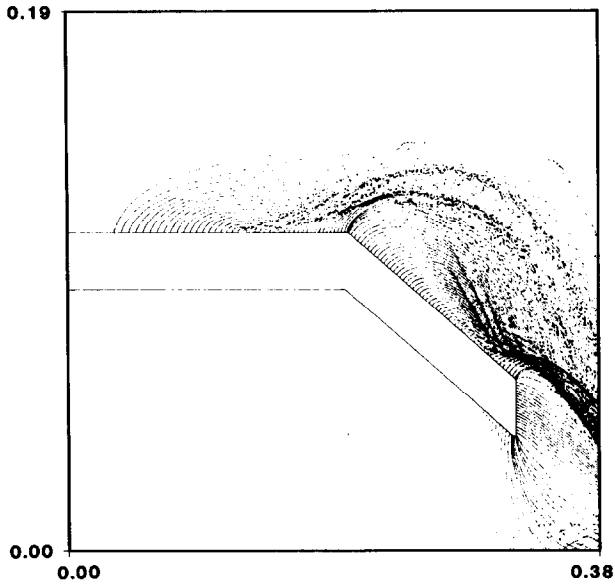

FIG. 10. Electron trajectory plot of the HELIA diode simulation at $t = 10$ ns.

accurately model the behavior there. To verify charge conservation, a diagnostic was added to monitor $(\nabla \cdot \mathbf{D} - \rho)$ on the grid and also the time history of the quantity

$$\Delta Q_{\max} = \frac{\max\{\nabla \cdot \mathbf{D} - \rho\}}{\max\{\rho\}},$$

where $\max\{x\}$ is the maximum value of x over all full grid points. This run was made on a machine with 14 digit precision, and after 5000 time steps, $\Delta Q_{\max} \simeq 2 \times 10^{-11}$, which is strong evidence that a charge is being conserved to machine roundoff levels. Finally, the radial profile of the current at the anode shows that half the current is within a disk of radius 6 cm, in fair agreement with experiment.

VI. SUMMARY

The tests indicate that the new slanted conducting surface and field emission models are working well. The slanted surface Child–Langmuir tests indicate that emission from slanted surfaces results in errors comparable to emission from conformal surfaces, at least for that problem. Finally, the HELIA diode simulation more fully illustrates the code's capabilities. Electromagnetic boundary conditions and particle emissions are modeled at slanted surfaces and corners in a complex geometry, while conserving charge to within machine precision.

ACKNOWLEDGMENTS

I wish to thank David Seidel and James Poukey for useful discussions and assistance in performing the HELIA diode simulations.

REFERENCES

1. M. E. JONES, "Electromagnetic PIC Codes with Body-Fitted Coordinates," 12th Conference on the Numerical Simulation of Plasmas, San Francisco, CA, Sept. 20–23, 1987 (unpublished).
2. D. SELDNER AND T. WESTERMANN, *J. Comput. Phys.* **79**, 1 (1988).
3. B. GOPLEN, R. E. CLARK, J. MCDONALD, AND W. M. BOLLEN, Mission Research Corp. Report No. MRC/WDC-R-068, 1983 (unpublished).
4. E. KALNAY DE RIVAS, *J. Comput. Phys.* **10**, 202 (1972).
5. C. K. BIRDSALL AND A. B. LANGDON, *Plasma Physics via Computer Simulation* (McGraw–Hill, New York, 1985), Chaps. 14 and 15.
6. R. L. MORSE AND C. W. NIELSON, *Phys. Fluids* **14**, 830 (1971).
7. T. D. POINTON, Sandia National Laboratory Report No. SAND88-0982, 1988 (unpublished).
8. J. P. QUINTENZ, *J. Appl. Phys.* **49**, 4377 (1978).
9. R. B. MILLER, *An Introduction to the Physics of Intense Charged Particle Beams* (Plenum, New York, 1982), p. 34.
10. A. PALEVSKY, Ph.D. thesis, Massachusetts Institute of Technology, June 1980 (unpublished).
11. M. R. SPIEGEL, *Mathematical Handbook* (McGraw–Hill, New York, 1968), p. 37.
12. I. LANGMUIR, *Phys. Rev.* **4**, 238 (1931).
13. T. W. L. SANFORD *et al.*, *J. Appl. Phys.* **63**, 681 (1988).